Polymer 50 (2009) 4727–4736

Contents lists available at ScienceDirect

Polymer

journal homepage: www.elsevier.com/locate/polymer

Shear-induced phase separation and crystallization in semidilute solution of ultrahigh molecular weight polyethylene: Phase diagram in the parameter space of temperature and shear rate

Hiroki Murase [a,b], Yasuo Ohta [b], Takeji Hashimoto [a,c,*]

[a] Department of Polymer Chemistry, Graduate School of Engineering, Kyoto University, Katsura, Nishikyo-ku, Kyoto 615-8510, Japan
[b] Research Center, TOYOBO Co., Ltd., 2-1-1, Katata, Ohtu-shi, Shiga 520-0292, Japan
[c] Advanced Science Research Center (ASRC), Japan Atomic Energy Agency (JAEA), Tokai-mura, Naka-gun, Ibaraki 319-1195, Japan

ARTICLE INFO

Article history:
Received 16 February 2009
Received in revised form
1 June 2009
Accepted 20 June 2009
Available online 26 June 2009

Keywords:
Shear-flow-induced structure
Phase separation
Crystallization

ABSTRACT

In the previous papers, we elucidated enhancement of concentration fluctuations, phase separation, and crystallization induced by steady state or step-up shear flow, as observed by shear small-angle light scattering, optical microscopy, and birefringence, for a semidilute solution of ultrahigh molecular weight polyethylene in paraffin as an athermal solvent. However the studies were done only at a given temperature of 124 °C, which is higher than the nominal melting temperature of the quiescent solution T_{nm} (115–119 °C). It is crucial to extend the studies over a wider temperature range in order to generalize shear-induced phase behavior of the solution. Thus in this work we constructed a kind of phase diagram in the parameter space of temperature (T) and shear rate ($\dot{\gamma}$). The temperature range covered was higher than T_{nm}, so that the phase diagram is strictly concerned with shear-induced phase behavior (i.e., without shear the solution is homogeneous and in a single-phase state). The diagram identified Regimes I–III in the T–$\dot{\gamma}$ space as will be detailed in the text. In constructing the phase diagram we found the following new points also. (i) The critical shear rate $\dot{\gamma}_{cx}$ which defines the boundary between Regimes I and II was independent of T. (ii) Regime III identified previously through the $\dot{\gamma}$ dependence of the integrated scattered intensity only at a particular temperature $T = 124$ °C was further separated into two regimes of III_a and III_b below and above a critical temperature (147 °C), respectively, through the observation of the $\dot{\gamma}$ dependence as a function of T: In Regime III_a, the sheared solution developed the optically anisotropic fibrous structures, indicative of the shear-induced crystallization triggered by the shear-induced concentration fluctuations in Regime II; In Regime III_b, the solution is so stable that it did not show a trend of the shear-induced crystallization even at the highest shear rates accessible in this experiment, but it only showed the shear-induced phase separation. (iii) The critical shear rates $\dot{\gamma}_{c,streak}$ and $\dot{\gamma}_{cz}$, which define respectively the boundary between Regimes II and III_a and that between Regimes II and III_b, are sensitive to temperature.

1. Introduction

In the previous paper [1] we elucidated that the shear-induced crystallization occurs after the shear-induced phase separation for a semidilute solution of ultrahigh molecular weight polyethylene (UHMWPE) by the simultaneous measurements of shear small-angle light scattering (shear-SALS), birefringence, and transmission optical microscopic images with increasing shear rate $\dot{\gamma}$. The studies, however, were conducted only at a particular temperature of 124 °C above its nominal melting temperature T_{nm} (115–119 °C, depending on isothermal crystallization temperatures) and close to equilibrium melting temperature for the quiescent solution. Although the studies elucidated fundamental results on self-assembly of dissipative structures (ordered structures developed in open nonequilibrium systems [2]), the results obtained only at the given temperature T are very far from a satisfaction and completion.

In order to generalize the study, it is indispensable to extend the temperature range covered by the experiments and to construct a kind of phase diagram for the shear-induced phase behavior of the solutions in the parameter space of T and $\dot{\gamma}$. Consequently in this paper we aimed to study the shear-induced structures for the same solutions as those studied earlier [1] as a function of T in order to construct the phase diagram in the T–$\dot{\gamma}$ space. There have been no reports so far on systematic studies of such phase diagram,

* Corresponding author. Professor Emeritus, Kyoto University, Japan.
E-mail address: hashi2@pearl.ocn.ne.jp (T. Hashimoto).

0032-3861/$ – see front matter © 2009 Elsevier Ltd. All rights reserved.
doi:10.1016/j.polymer.2009.06.049

despite of its importance. The lowest temperature limit (124 °C) was deliberately fixed on the basis of the following fact. The crystallization above this temperature limit does not practically occur in the quiescent solution. If the crystallization occurs, it occurs only due to the influence of shear flow; Without the shear, the solution is perfectly homogeneous and in a single-phase state.

When semidilute polymer solutions in a single-phase state are subjected to shear flow with flow rates larger than a critical value, the solutions become turbid because of the liquid–liquid phase separation or the enhancement of concentration fluctuations induced by the flow [3–5] via elastic deformation of polymer chains [6–8]. The shear-induced phase separation or the enhancement of concentration fluctuations has been well studied *in-situ* by shear-SALS for semidilute solutions of noncrystallizable polymers, for example atactic polystyrene/dioctylphthalate solutions (PS/DOP) [2,9–14].

This intriguing phenomenon has been studied also for semidilute solutions of crystallizable polymers, e.g., UHMWPE solutions [1,15–17]. In this system one must generally consider the shear-induced crystallization in addition to the shear-induced phase separation or the enhancement of concentration fluctuations driven by the elastic effect. As a matter of fact it is well known that formation of fibrous crystals having a characteristic morphology of the so called "shish–kebab" is a general phenomenon found in dilute, semidilute solutions, and melt of polyethylene under various flow fields such as shear, extensional, and mixed flow [18–23].

A great number of works have been conducted to elucidate the mechanism of the shish–kebab formation. However, the mechanism is not perfectly clarified up to the present date. Keller [24] firstly pointed out that the coil-stretch transition, which was theoretically predicted by de Gennes [25], plays an important role on the flow-induced crystallization. He demonstrated an abrupt change in birefringence, indicative of an appearance of the fully extended chains above a critical strain rate in dilute solution under extensional flow. Many researchers have been stimulated by his work, and many experimental [26–31] and simulation [32] works have been carried out in order to obtain the certain evidence of the transition acting as a driving force of the flow-induced crystallization. Many researchers have adopted polymer melts, especially chosen binary melt blends of high and low molecular weight polymers, as samples to elucidate the hypothesis and obtained experimental results suggesting that the coil-stretch transition occurring in the section of chains between the entanglements primarily affects the flow-induced crystallization [26–29,31].

However, we should emphasize again that not only the coil-stretch transition but also the shear-induced phase separation plays an important role on the flow-induced crystallization for polymer solutions and for the binary melt blends having a sufficiently large molecular weight difference. We actually found [1] that: upon increasing $\dot{\gamma}$ at 124 °C, the shear-induced phase separation occurs first; it then triggers the shear-induced crystallization, giving rise to a depolarized streak-type shear-SALS pattern extended perpendicular to the flow direction. This pattern implies formation of the optically anisotropic fibrous structures along the flow direction.

At this particular temperature (124 °C), we elucidated that the shear-induced structures on the UHMWPE solution at the steady state can be classified into the following three shear regimes [1]: Regime I where the solution is kept to be homogeneous even under the flow, Regime II where the shear enhances the plane-wave type concentration fluctuations with their wave vectors preferentially oriented parallel to the flow direction, and Regime III where a series of the following transient events occur to eventually create the optically anisotropic string-like or fibrous structure upon increasing $\dot{\gamma}$ from Regimes II to III. The events consist of the transformation of the plane-wave type concentration fluctuations into demixed domains rich in polymer dispersed in the medium of polymer-poor solution, alignment of demixed domains into string-like structures oriented parallel to the flow direction, and then crystallization of the string-like structure in order of increasing shear rate [1,16,33].

In this paper we aim to (i) identify Regimes I–III as a function of temperature to construct the T–$\dot{\gamma}$ phase diagram and to (ii) investigate T dependence of the critical shear rates between Regimes I and II and that between Regimes II and III. The elucidation will be useful to clarify further relations between the shear-induced phase separation and the shear-induced crystallization at various temperatures other than 124 °C. Moreover, we aim to compare characteristic features of the PE solutions to those of well studied semidilute solutions of the noncrystallizable polystyrene (PS) solutions [2,14,33].

2. Sample and experimental method

2.1. Sample

A commercial grade UHMWPE (Hizex 240 M, Mitsui Chemicals, Tokyo, Japan) was used for this experiment as a solute. The polymer has a weight-average molecular weight of $M_w = 2.0 \times 10^6$ and heterogeneity index $M_w/M_n = 12$, where M_n denotes the number-average molecular weight. Paraffin wax (Luvax 1266: Nippon Seiro Co., Ltd., Tokyo, Japan) was used as a solvent. We used the polymer having a broad molecular weight distribution in this work, simply because it is readily available and commercially important. The molecular weight of the paraffin wax is approximately 500 (producer's specification; measured by gas chromatography) and its melting point is 69 °C. The UHMWPE was dissolved in the paraffin wax with an antioxidant agent (2,6-di-*tert*-butyl-*p*-cresol), by an amount of 1 wt% of the total solution, using a screw type extruder at 210 °C. Small particles contaminating the solutions were filtered off by a mesh filter (400 line/inch). This filtration process was highlighted to be very important for obtaining reliable scattering data on the shear-induced structures and scattering in our previous works [15]. A 5 wt% solution having c/c^* of approximately 11 was prepared (c^* is overlap concentration). The equilibrium melting temperature T_d^0 of crystals in the solution was estimated to be 124 ± 1 °C by Hoffman–Weeks plot [34] as detailed elsewhere [1]. Nominal melting temperature of the solution is 115–119 °C which depends on isothermal crystallization temperatures of the solution [1].

2.2. Shear small-angle light scattering (shear-SALS)

The shear-SALS experiments were carried out using a laboratory-made apparatus in Kyoto University to record the scattering patterns with a CCD camera and a Macintosh computer system and to measure the scattered intensity with one-dimensional photodiode array system [35,36]. The optical setup of the apparatus was identical to those described in the previous reports [1,15,16]. We used a cone-plate type shear cell made out of quartz having the cone angle of 1°. The conventional coordinate system was used as depicted in Fig. 1. The flow, velocity gradient, and neutral (or vorticity) directions are taken along the O*x*-, O*y*- and O*z*-axis, respectively. All the scattering patterns were observed on the O*xz* plane.

3. Experimental results and discussion

3.1. Steady-state scattering patterns as a function of shear rate and temperature

Shear-SALS experiments were performed at various shear rates from 0.029 to 740 s^{-1} and at temperatures from 124 to 150 °C. The shear flow at a given shear rate was imposed on the solution at rest

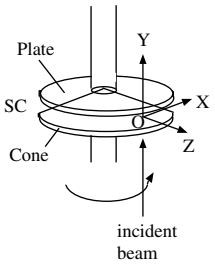

Fig. 1. Schematic illustration of a cone-and-plate shear cell (SC) and the Cartesian coordinate system O*xyz*. O*x*-, O*y*- and O*z*-axis are the flow direction, the velocity gradient direction, and the vorticity direction, respectively. The incident beam was sent along the O*y*-axis.

and the constant shear rate was kept until when the intensity of the scattering pattern reached steady state. The scattering pattern projected on a screen placed normal to the O*y*-axis was recorded by a CCD camera (Fig. 2). The incident beam has a polarization direction parallel to the O*z*-axis, and an analyzer was not used between the sample and the detector throughout this work. Fig. 2 shows the scattering patterns thus taken at various shear rates and temperatures.

Fig. 2 elucidates the shear-induced phase behavior of the UHMWPE solutions as observed by the shear-SALS patterns over the wide T and $\dot{\gamma}$ range. It unveils the areas for Regimes I, II and III where Regime III is newly found to be composed further of III_a and III_b in the T–$\dot{\gamma}$ parameter space. Although the characteristics of the SALS patterns and the shear-induced structures in these regimes except for III_b are already described elsewhere [1], they are briefly described below. In Regime I, the scattering pattern is the same as that from the quiescent solution, so that the solution is homogeneous even under the shear flow. In Regime II, the sheared solution exhibits the butterfly type scattering pattern extended along the O*x* direction, indicative of shear-enhanced concentration fluctuations. It turns out that Regime III defined in the previous work [1] through the observation of the $\dot{\gamma}$ dependence of the integrated scattered intensity only at $T = 124\,^{\circ}C$ should be further classified into III_a and III_b below and above 147 °C, respectively by the present investigation as a function of T. Regime III_a, which was defined as Regime III in the previous work [1], the characteristic streak pattern extended along the neutral direction (the O*z* direction) was developed in addition to the butterfly pattern extended along the flow direction (O*x* direction). The streak pattern, which is also observed under crossed polarizers, indicates an evolution of optically anisotropic string-like or fibrous structure as described earlier in section I. The critical shear rate $\dot{\gamma}_{c,streak}$ for the onset of development of the streak pattern in Regime III_a seems to increase with increasing T, which will be more quantitatively discussed later in the Section 3.2. However at $T \geq 148\,^{\circ}C$, the streak pattern extended along the O*z* direction was never observed with increasing $\dot{\gamma}$ even at the highest $\dot{\gamma}$ covered in this experiment. Instead we observed only the butterfly pattern plus the enhanced intensity along the O*z* direction at $\dot{\gamma} \geq \dot{\gamma}_{cz}$, seemingly due to the demixed domains. The critical shear rate $\dot{\gamma}_{cz}$ will be defined later more clearly in Section 3.2 in conjunction with Fig. 5. The scattering patterns in Regime III_b correspond to those observed in Regime III for the PS/DOP solutions [14].

Fig. 3 demonstrates scattering patterns taken at 146 °C and 148 °C as a function of $\dot{\gamma}$ in order to compare $\dot{\gamma}$-dependence of the pattern in these two temperature regions (III_a and III_b). At 146 °C in Regime III_a, a very weak but obvious streak pattern is observed at $\dot{\gamma} = 29\ s^{-1}$ (Fig. 3a). With increasing $\dot{\gamma}$, the streak pattern became stronger and clearer as shown in Fig. 3b–d. On the other hand at 148 °C in Regime III_b, the streak pattern could not be observed even at shear rates much higher than that applied to the solution at 146 °C (Fig. 3g and h). The scattered intensity perpendicular to the

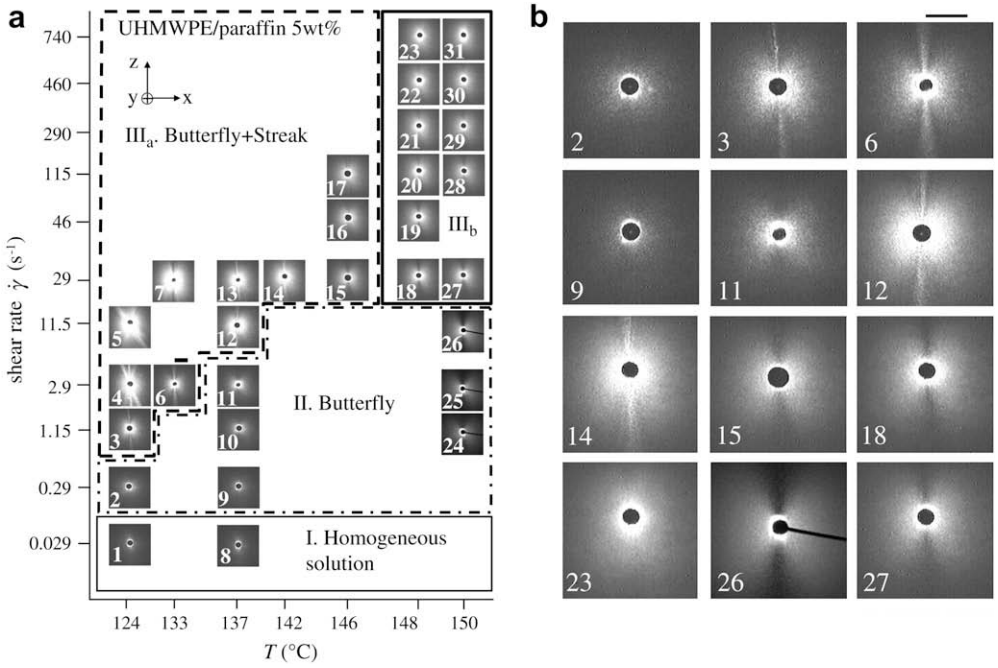

Fig. 2. A phase diagram for shear-induced structure in the shear rate ($\dot{\gamma}$)–temperature (T) parameter space which shows typical shear-induced scattering patterns in the O*xz* plane (part a) and some representative scattering patterns in part (a) (part b). The flow direction is horizontal. The scale bar attached to the pattern (#6) is $q = 5.2 \times 10^{-4}\ nm^{-1}$ and is common for all the patterns in this figure. The scattering patterns classified the solution into the following four regimes. (I) The homogeneous solution encompassed by the solid line, (II) the solution giving rise to butterfly pattern (encompassed by the dash–dot line), and (III_a) the solution giving rise to butterfly pattern plus the streak pattern extended along the O*z*-axis, and (III_b) the solution giving rise to the butterfly pattern plus the shear-enhanced scattering along the neutral direction (the O*z*-axis), hence having shear-induced demixed domains. Regime III_a is encompassed by the dashed line, while Regime III_b is encompassed by the solid line. The number attached to the patterns in part (b) corresponds to that in part (a).

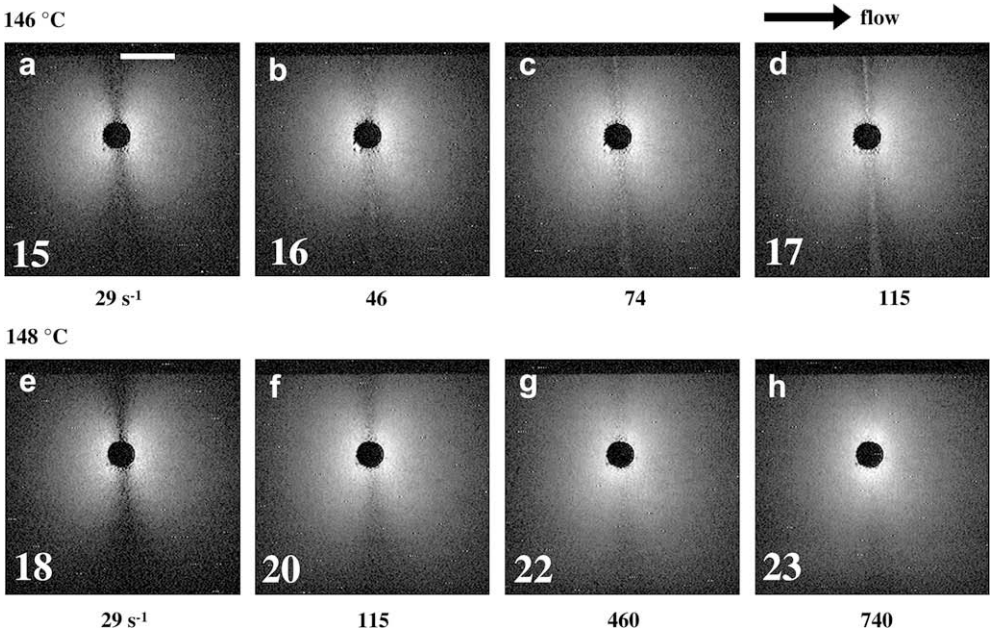

Fig. 3. Comparison of the patterns at 146 °C and 148 °C. The numbers indicated in left-bottom of each pattern correspond with those indicated in each pattern in Fig. 2. The flow direction is horizontal and the scale bar in the pattern (a) is $q = 5.2 \times 10^{-4}$ nm^{-1} which is common to all the patterns. The upper series represent the patterns obtained at 146 °C: (a) $\dot{\gamma} = 29$ s^{-1}, (b) 46 s^{-1}, (c) 74 s^{-1}, (d) 115 s^{-1}. The lower series represents the patterns obtained at 148 °C: (e) 29 s^{-1}, (f) 115 s^{-1}, (g) 460 s^{-1}, (h) 740 s^{-1}.

flow direction, however, became stronger and the dark streak of the butterfly pattern [9,12] became ambiguous with increasing shear rate. At $\dot{\gamma} = 740$ s^{-1} (Fig. 3h) which is close to an upper limit of the shear rate accessible in this experiment, the feature of butterfly pattern is recognized only at higher scattering angles and the pattern in lower scattering angles became elliptical with its major axis perpendicular to the flow direction, indicative of the trend for the formation of the string-like structure. Therefore we shall classify the high T ($T \geq 148$ °C) and high $\dot{\gamma}$ ($\dot{\gamma} \geq 29$ s^{-1}) region as Regime III$_b$. This regime newly found in this work will be later discussed in detail in conjunction with Fig. 5.

3.2. Scattered intensity as a function of shear rate at various temperatures

Fig. 4 shows the integrated scattered intensities parallel and perpendicular to the flow direction, $\mathcal{I}_{\parallel}$ and $\mathcal{I}_{\perp}$, respectively, as a function of $\dot{\gamma}$ at 124 °C and 133 °C where $\dot{\gamma}$ was stepwisely increased. The birefringence data Δn_{x-z} (filled triangles) obtained at 124 °C, shown on the right ordinate axis, will be explained later in Section 5. $\mathcal{I}_{\parallel}$ and $\mathcal{I}_{\perp}$ were obtained by integrating the scattered intensity over a given q-range (from $q = 3.0 \times 10^{-4}$ nm^{-1} to 2.6×10^{-3} nm^{-1}), where q is defined as $q = (4\pi/\lambda)\sin(\theta/2)$ with θ and λ being scattering angle and wavelength of the incident beam, both in the medium, respectively. The reduced integrated intensity was obtained by normalizing the integrated intensity at a given $\dot{\gamma}$ with that at quiescent state $\mathcal{I}_{\parallel}$ ($\dot{\gamma} = 0$) or $\mathcal{I}_{\perp}$ ($\dot{\gamma} = 0$). At these temperatures, the solution passes through Regimes I, II and III$_a$ with increasing $\dot{\gamma}$.

In Regime I, both $\mathcal{I}_{\parallel}$ and $\mathcal{I}_{\perp}$ kept almost the same value as that of quiescent solution, indicating that the concentration fluctuations of the solution are unaltered with $\dot{\gamma}$. In the range of $\dot{\gamma} \geq \dot{\gamma}_{cx}$ defined as Regime II, a shear-enhanced scattering obviously occurs along the flow direction as shown by the increase of $\mathcal{I}_{\parallel}$ and by the appearance of characteristic "butterfly" pattern. However, the intensity $\mathcal{I}_{\perp}$ is still kept approximately the same value as that of quiescent solution. This clearly indicates that the shear enhances selectively the Fourier mode of concentration fluctuations (as represented by plane waves) with their wave vectors preferentially oriented parallel to the flow direction. The value of $\dot{\gamma}_{cx}$ was about the same at 124 °C and 133 °C within an experimental error. At $\dot{\gamma} \geq \dot{\gamma}_{c,streak}$, the intensity $\mathcal{I}_{\perp}$ dramatically increased, reflecting development of the streak pattern in Regime III$_a$. The subscript "a" was added to distinguish this regime from that of Regime III$_b$ occurring even at higher temperatures as will be clarified below. The critical shear rate $\dot{\gamma}_{c,streak}$ at 133 °C was remarkably higher

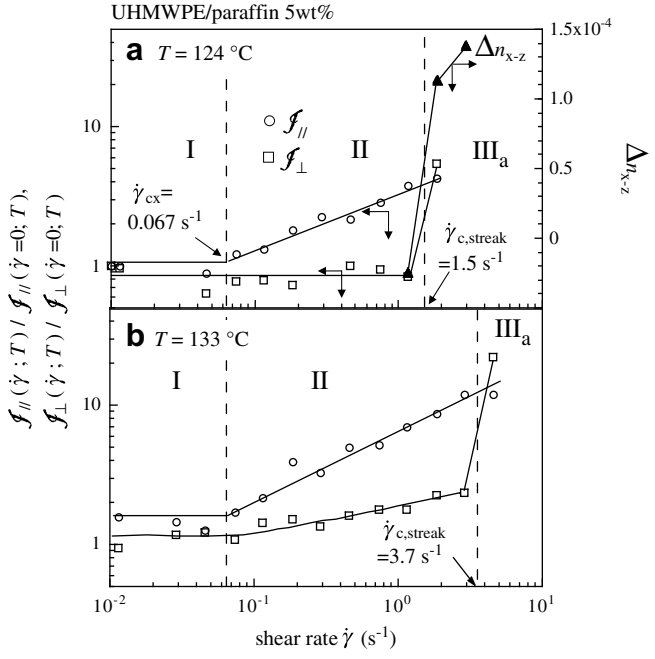

Fig. 4. Reduced integrated scattered intensity parallel and perpendicular to shear flow $\mathcal{I}_{\parallel}(\dot{\gamma};T)/\mathcal{I}_{\parallel}(\dot{\gamma}=0;T)$ and $\mathcal{I}_{\perp}(\dot{\gamma};T)/\mathcal{I}_{\perp}(\dot{\gamma}=0;T)$, respectively, as a function of shear rate $\dot{\gamma}$ at 124 °C (a) and 133 °C (b). Part (a) indicates $\dot{\gamma}$ dependence of birefringence Δn_{x-z} also in the right ordinate.

than that of 124 °C, which is consistent with the tendency observed in Fig. 2.

Fig. 5 shows $\mathcal{I}_{\parallel}$ and $\mathcal{I}_{\perp}$ as a function of $\dot{\gamma}$ at 150 °C. The data of the integrated scattered intensity measured by the CCD camera (filled symbols) were also added to those measured by the photodiode array system (unfilled symbols). Behavior of the scattering pattern in Regimes I and II was essentially the same as those observed at the lower temperatures shown in Fig. 4. The $\dot{\gamma}_{cx}$ at this temperature was 0.065 s^{-1} which is almost the same value as that obtained at the lower temperatures. We shall discuss later the temperature dependence of $\dot{\gamma}_{cx}$ in Section 5. At $\dot{\gamma} \geq \dot{\gamma}_{cz}$, the $\mathcal{I}_{\perp}$ began to *gradually* increase with increasing shear rate toward the intensity level of $\mathcal{I}_{\parallel}$ at the highest $\dot{\gamma}$, on the contrary to the *steep* increase of $\mathcal{I}_{\perp}$ at $\dot{\gamma} > \dot{\gamma}_{c,streak}$ at the lower temperatures (Fig. 4). The regime where $\mathcal{I}_{\perp}$ starts to increase was defined as Regime III_b in order to distinguish the scattering behavior in this regime from that in Regime III_a. This regime III_b corresponds to Regime III in the noncrystallizable PS/DOP solutions [12,14] (see Fig. 9a to be described later in Section 5). The enhanced $\mathcal{I}_{\perp}$ in Regime III_b is expected to be a consequence of presence of the demixed domains [37]. Moreover the increase of $\mathcal{I}_{\perp}$ close to $\mathcal{I}_{\parallel}$ at $\dot{\gamma} = 740\ s^{-1}$ (the highest $\dot{\gamma}$) shows the trend toward formation of the string-like structure as pointed out in Section 3.1.

Fig. 6 presents the phase diagram summarizing the shear-induced scattering behavior shown in Figs. 2–5 in the T–$\dot{\gamma}$ parameter space. Numbers attached to the symbols correspond with the numbers attached to each scattering pattern in Fig. 2. Four symbols, i.e., circles, triangles, squares, and diamonds, denote the state of the sheared solution as assessed from the scattering behavior. The filled and the unfilled marks represent the scattering data obtained with the photodiode array system and the CCD camera system, respectively. The circles denote the homogeneous solution in Regime I. The triangles denote Regime II which exhibits the plane-wave type shear-enhanced concentration fluctuations as characterized in Figs. 4 and 5. The half-filled and half-unfilled triangles denote the shear-enhanced concentration fluctuations as identified by both CCD camera and the photodiode array, respectively. The critical shear rate $\dot{\gamma}_{cx}$ (T) as a function of T is depicted by the thin solid line in Fig. 6: $\dot{\gamma}_{cx}$ appears to be almost independent of T within the range of temperature covered in this experiment.

In Regime III_a at $\dot{\gamma} > \dot{\gamma}_{c,streak}$ and $T \leq 146$ °C, the streak pattern was developed. The squares denote observed data points in Regime III_a. The thick solid line and the broken line in Fig. 6 represent the $\dot{\gamma}_{c,streak}$ (T). A small discrepancy between these two lines comes from the difference in the experimental condition as mentioned in

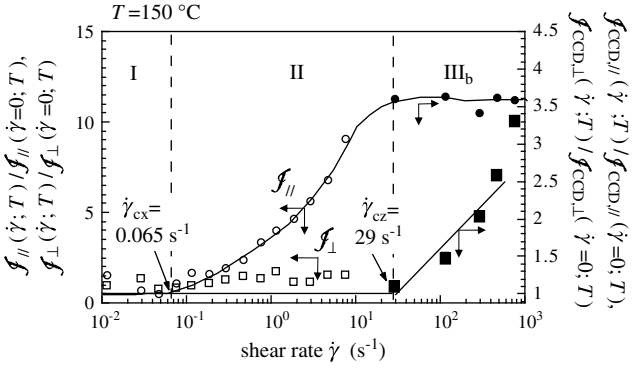

Fig. 5. Reduced integrated scattered intensity parallel and perpendicular to shear flow $\mathcal{I}_{\parallel}(\dot{\gamma};T)/\mathcal{I}_{\parallel}(\dot{\gamma}=0;T)$ and $\mathcal{I}_{\perp}(\dot{\gamma};T)/\mathcal{I}_{\perp}(\dot{\gamma}=0;T)$, respectively, as a function of shear rate at 150 °C. The integrated scattered intensity measured by the CCD camera (filled symbols) was added to that measured by the photodiode array system (unfilled symbols).

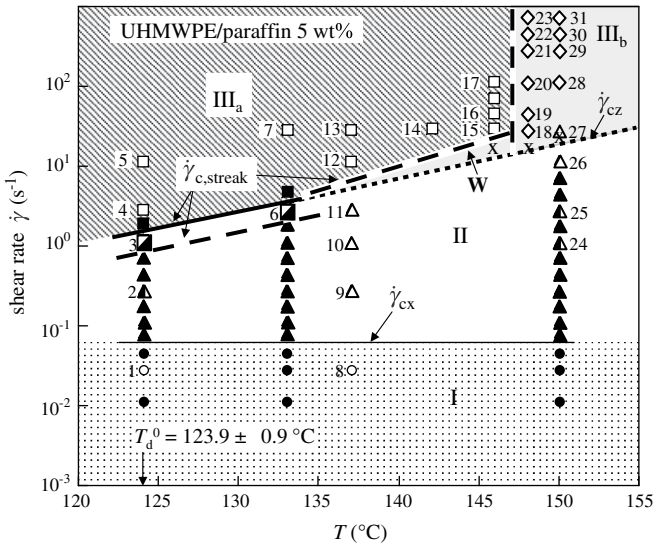

Fig. 6. Phase diagram obtained from the scattering behaviors as a function of temperature and shear rate. Numbers put beside the marks correspond with those attached to each scattering pattern in Fig. 2. Four marks, i.e., circles, triangles, squares, and diamonds denote the state of the solution classified by the scattering behavior. The unfilled and the filled marks represent the data taken by the CCD camera and the photodiode array system, respectively. The detailed description about the classification of the regimes is presented in the text.

References [38]: a multi-step (thick solid line) and single-step (broken line) increase of shear rate to the given shear rate.

The highest temperature limit, where the streak-like pattern was formed under shear flow, was found to be 146 °C. At temperatures equal to or higher than 148 °C, we could not observe the obvious streak pattern even at shear rates close to 1000 s^{-1}. The data marked by diamonds in Fig. 6 denote the region where only the butterfly pattern was observed in the 2D-SALS (see Fig. 3e–h). The dotted line characterizing the boundary between Regimes II and III_b represents $\dot{\gamma}_{cz}$ (T) defined in Fig. 5. $\dot{\gamma}_{cz}$ ($T = 146$ °C), $\dot{\gamma}_{cz}$ ($T = 148$ °C), and $\dot{\gamma}_{cz}$ ($T = 150$ °C) denoted by the symbol of cross in Fig. 6 were estimated as the shear rates at the onset of increase of $\mathcal{I}_{\perp}$ with increasing $\dot{\gamma}$ by using the method as already indicated in conjunction with Fig. 5. A main part of Regime III_b exists in the parameter space defined by $\dot{\gamma} > \dot{\gamma}_{cz}$ and $T > 146$ °C. A further detail of this regime (including the dash–dot line) will be described later in Section 5.

4. Scattering behavior after cessation of shear flow in various regimes in T–$\dot{\gamma}$ space

As we have already shown in the previous papers [1,16], though these papers were concerned with the results only one particular temperature at 124 °C, the change in scattering behavior after cessation of shear flow turned out to give a fruitful insight into the structure developed under the shear flow. All the scattering patterns developed in Regimes II and III_b, regardless of the applied temperatures and shear rates, relax to the same pattern as that for the quiescent solution after the cessation of shear flow. The decay of the butterfly pattern after the cessation indicates that the structure giving rise to the butterfly pattern should be attributed to the concentration fluctuations or phase separation developed under shear flow. On the contrary, the scattering patterns developed in Regime III_a remained unrelaxed, for some periods of time or for ever, even after the cessation of the shear flow.

Fig. 7 presents typical scattering patterns observed at 600 s after the cessation of shear flow in Regime III_a where the number attached to each pattern corresponds to that shown in Fig. 2 or 6

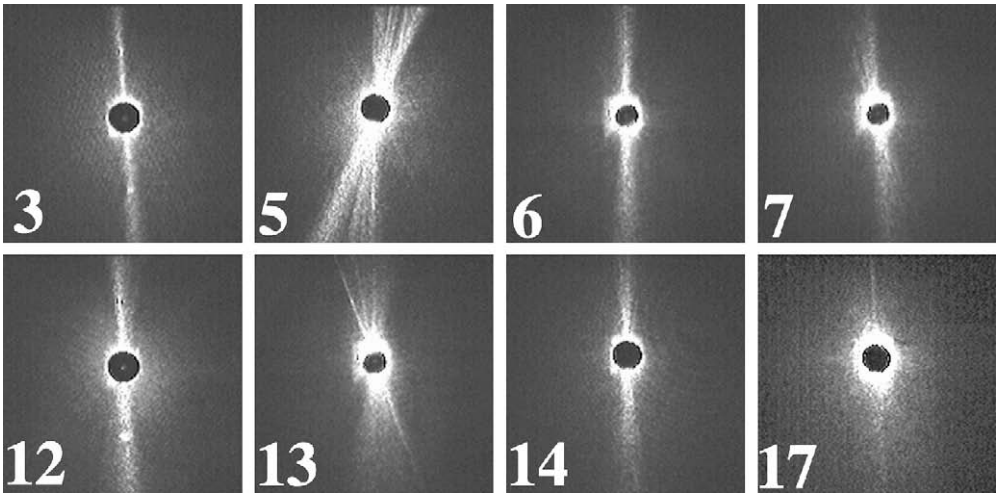

Fig. 7. Scattering patterns observed after cessation of shear flow for the solution sheared originally at a given set of temperature and shear rate in Regime III_a. The numbers indicated in left-bottom of each pattern correspond with those indicated in each pattern in Fig. 2 or 6. The scattering patterns for the solutions sheared in Regimes I, II, and III_b (defined in Fig. 6) recovered the same pattern as that for the quiescent solution, so that the patterns were not included in the figure.

and hence specifies the set of parameters ($\dot{\gamma}$, T) describing the steady-state shear flow achieved before the shear cessation. This figure should be compared with Fig. 2 for the steady-state scattering patterns before the cessation. After the cessation of shear flow in Regime III_a, the streak-like scattering pattern remained at 600 s, although the butterfly type scattering pattern superposed on the streak completely disappeared at 600 s.

Therefore we can find out that the previous conclusion on Regime III obtained only at 124 °C is applicable to all the temperatures in Regime III_a. This suggests that the structure giving rise to the streak pattern in the shear-SALS patterns at all the temperatures in Regime III_a may result from shear-induced crystallization into fibrous structures and that the structure cannot be relaxed or can be relaxed slowly into homogeneous solution after the cessation, depending on temperatures at which shear is imposed on the solution. The results further imply that the conclusion obtained at 124 °C, concerning the shear-induced phase separation being followed by the shear-induced crystallization, can be applicable to all the temperatures in Regime III_a.

It is important to note here that: the streak-like scattering pattern observed *in-situ* under the shear flow is fluctuating, giving rise to multiple streaks or a single streak; the orientation of the streak pattern changes around the neutral axis by about 20° at a maximum. The result implies that the string-like structures developed under the shear flow exist under such a dynamic equilibrium that the structures grow but overgrown structures are disrupted. The structures developed may have a solid-like integrity (or some crystallinity) and hence be subjected to lateral forces originating from normal forces developed in the sheared solution. The lateral forces may account for the orientation fluctuations of the string-like structures with respect to the flow direction and hence for the orientation fluctuations of the streak-like pattern with respect to the neutral direction. The fluctuations of the streak-like pattern were never observed in the noncrystallizable polymer solution, PS/DOP, probably because the string formed in the system is not solid-like.

Fig. 8 demonstrates time changes in the scattered intensity after cessation of the steady-state shear flow for the sheared solution in Regime III_a. The $\mathcal{J}_{total}(t_{cess.})$, the scattered intensity integrated over the whole area of the CCD image, was measured as a function of time $t_{cess.}$ after the shear cessation. The area covered were $|q_x| \leq 1.96 \times 10^{-3}\ nm^{-1}$ and $|q_z| \leq 1.87 \times 10^{-3}\ nm^{-1}$, excluding the

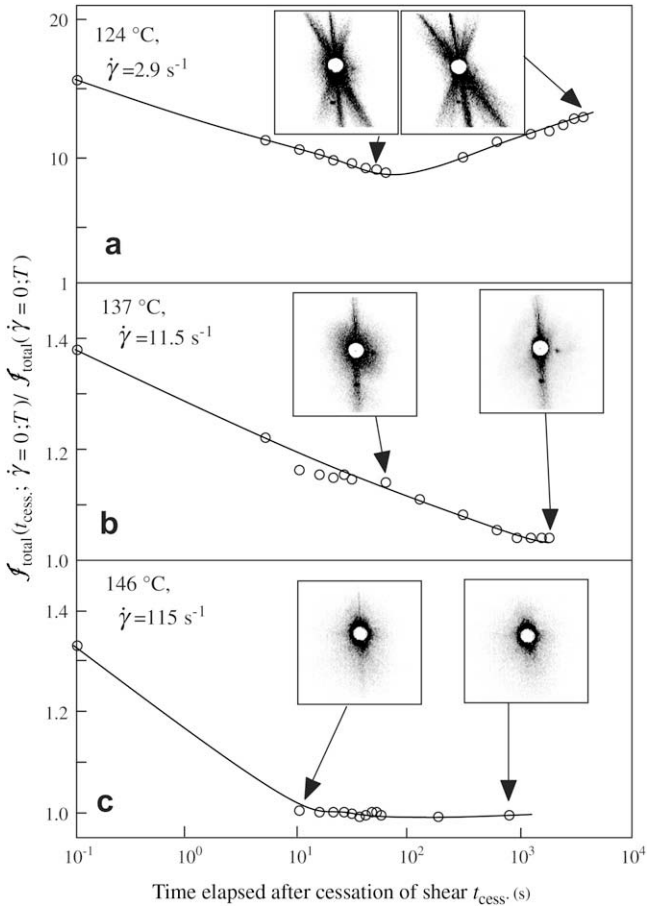

Fig. 8. Time changes in scattered intensity and scattering pattern as a function of time $t_{cess.}$ elapsed after cessation of the steady shear flow. The scattered intensity $\mathcal{J}_{total}(t_{cess.})$ integrated over the whole area of the CCD was measured as a function of time $t_{cess.}$. $\mathcal{J}_{total}(t_{cess.})$ was normalized with the integrated scattered intensity $\mathcal{J}_{total}(\dot{\gamma}=0)$ for the quiescent solution before onset of the shear flow: (a) at 124 °C and at $\dot{\gamma}=2.9\ s^{-1}$; (b) at 137 °C and at $\dot{\gamma}=11.5\ s^{-1}$; (c) at 146 °C and at $\dot{\gamma}=115\ s^{-1}$.

beam stop area specified by $q \leq 0.9 \times 10^{-4}\,\mathrm{nm}^{-1}$. The scattered intensity $\mathcal{I}_{\mathrm{total}}(t_{\mathrm{cess.}})$ was normalized with the integrated scattered intensity $\mathcal{I}_{\mathrm{total}}$ $(\dot{\gamma}=0)$ of the quiescent solution. At 124 °C the intensity $\mathcal{I}_{\mathrm{total}}(t_{\mathrm{cess.}})$ first decreased with $t_{\mathrm{cess.}}$, due to the relaxation of the butterfly pattern, but subsequently turned into an increase, probably due to an increase of scattered intensity from the streak-like pattern as a consequence of growth of the fibrous structure due to crystallization at 124 °C. This result infers that the true equilibrium melting temperature of crystal in the solution is expected to be slightly higher than 124 °C estimated from the Hoffman–Weeks plot. Hence the crystals developed under the shear flow may serve as seeds for further crystallization after the shear cessation. At 137 and 146 °C higher than T_{d}^{0}, the streak pattern was remained for a period after the cessation. However, the integrated intensity eventually decreased toward that for the quiescent solution, due to disappearance of the streak pattern as a consequence of melting of the fibrous structure developed under the shear after the shear cessation. The relaxation time for the streak-like pattern, τ_{streak}, developed in the noncrystallizable PS/DOP solution (PS548/DOP 6.0 wt% at 25 °C) is smaller than the crystallizable PE/paraffin solution at 137 °C by about an order of magnitude. The larger τ_{streak} or the slower relaxation rate in the PE/paraffin solution than in the PS/DOP solution may be due to a contribution of melting of the crystals in the optically anisotropic string-like structure to τ_{streak}.

Before closing this section, we would like to note that a direct confirmation of the crystallization associated with the optically anisotropic string-like structures with a wide angle X-ray diffraction method (WAXD) is crucial. However only WAXD on the sheared solution is not sufficient. The WAXD should be conducted simultaneously with the SALS under the condition where the SALS exhibits streak-like pattern. This is an extremely difficult experiment but well deserves future works.

5. Comparison between sheared polystyrene solution and polyethylene solution

Comparisons of the shear-rate dependence of the steady-state scattering patterns for the PE solutions and the PS solutions, which represent crystallizable and noncrystallizable solutions respectively, elucidated the following differences:

(1) Temperature dependence of $\dot{\gamma}_{\mathrm{cx}}$ in the PE solution was smaller than that of the PS solution [39]. It is independent of temperature in the case of the PE solution.
(2) In the case of the PS solution we found both Regime III $(\dot{\gamma}_{\mathrm{cz}} < \dot{\gamma} < \dot{\gamma}_{\mathrm{a}})$ and Regime IV $(\dot{\gamma} > \dot{\gamma}_{\mathrm{a}})$ as reported earlier [40] and will be also shown in Fig. 9 later, but in the case of the PE solution we found Regimes III and IV degenerate into Regime III, comprising $\mathrm{III_a}$ and $\mathrm{III_b}$.
(3) More specifically, Regime $\mathrm{III_a}$ in the PE solution occurred at $\dot{\gamma} > \dot{\gamma}_{\mathrm{c,streak}}$ and $T < 147$ °C and Regime $\mathrm{III_b}$ occurred at $\dot{\gamma} > \dot{\gamma}_{\mathrm{cz}}$ and $T \geq 147$ °C and in the wedge-like region labeled by W in Fig. 6.

These differences in the scattering behavior between the PE solution and the PS solution must be caused by the differences of these systems in terms of both the rheological properties and the thermodynamic interactions between polymers and solvents. Moreover, the crystallizable nature of PE must be responsible for the differences, especially for the differences in (2) and (3).

The difference (1) may be interpreted as follows. We can predict the critical shear rate $\dot{\gamma}_{\mathrm{cx}}$ [39] according to the linearized theory of the shear-induced concentration fluctuations based on a two-fluid model [6–8]. The theoretical value of $\dot{\gamma}_{\mathrm{cx}}$, $\dot{\gamma}_{\mathrm{cx,theory}}$, is given by [8]

$$\dot{\gamma}_{\mathrm{cx,theory}} \cong K_{\mathrm{os}}/5\eta_0 \tag{1}$$

where K_{os} is the osmotic modulus, and η_0 is the zero shear viscosity. Equation (1) indicates that $\dot{\gamma}_{\mathrm{cx}}$ depends on the temperature through the temperature dependence of K_{os} and η_0. For a semidilute polymer solution, K_{os} has the following form:

$$K_{\mathrm{os}} = (k_{\mathrm{B}}T/\nu_0)\phi^2[\phi + (1-2\chi) + 1/(N_{\mathrm{n}}\phi)] \tag{2}$$

where k_{B} is the Boltzmann constant, ν_0 is the volume of monomeric unit, ϕ is the volume fraction of polymer, χ is the thermodynamic interaction parameter between polymer segments and solvents, N_{n} is the number-average polymerization index. η_0 is given by

$$\eta_0 \sim \exp(a/T) \tag{3}$$

Thus temperature dependence $\dot{\gamma}_{\mathrm{cx,theory}}$ arises from $k_{\mathrm{B}}T$ and χ in Eq. (2) and T in Eq. (3). In the temperature range covered in the PE and PS solutions under shear, absolute T hardly changes (factor of 1.07 even in the case of PE solution) so that the temperature dependence should primary arise from that of χ in Eq. (2). In the case of UHMWPE/paraffin system, χ must be almost zero, because the monomeric unit of UHMWPE and paraffin is chemically equivalent, forming an athermal solution. Thus K_{os} for the PE solution is almost independent of temperature compared with K_{os} for the PS solution, which account for the small temperature dependence of $\dot{\gamma}_{\mathrm{cx}}$ for the UHMWPE solution.

Now let us discuss the differences (2) and (3) as described above. We present a summary of the results obtained previously for the PS solutions in Fig. 9 in order to help readers to easily follow the discussion on the differences. Although the figure is based on our earlier publication [40], it contains a new finding also which was not previously pointed out. As elucidated previously, the sheared PS solution is classified into the four regimes, I to IV, across the critical shear rates $\dot{\gamma}_{\mathrm{cx}}$, $\dot{\gamma}_{\mathrm{cz}}$, and $\dot{\gamma}_{\mathrm{a}}$ as shown in Fig. 9. The critical shear rates $\dot{\gamma}_{\mathrm{cx}}$ and $\dot{\gamma}_{\mathrm{a}}$ are found to be closely related to the rheological relaxation rates τ_{m}^{-1} and τ_{e}^{-1} [41] where τ_{m} and τ_{e} are the longest rheological relaxation time and the chain retraction time ($\tau_{\mathrm{e}} = 2\tau_{\mathrm{R}}$, τ_{R} being the longest Rouse relaxation time), respectively. In Regime III for the PS solutions $(\dot{\gamma}_{\mathrm{cz}} < \dot{\gamma} < \dot{\gamma}_{\mathrm{a}})$, $\mathcal{I}_{\perp}(\dot{\gamma})$ started to increase from the value $\mathcal{I}_{\perp}(\dot{\gamma}=0)$ for the quiescent solution (Fig. 9a). The increase of $\mathcal{I}_{\perp}(\dot{\gamma})$ was considered to be a signature of shear-induced demixing [37], and hence of formation of the demixed domains rich in polymer chains in the matrix of the solvent-rich medium in Regime III. In the early stage in Regime IV for the PS solutions $(\dot{\gamma} \geq \dot{\gamma}_{\mathrm{a}})$, both $\mathcal{I}_{\parallel}$ and $\mathcal{I}_{\perp}$ further increased. The scattering pattern showed a strong streak-like scattering normal to the flow direction, superposed by the relatively weak butterfly pattern parallel to the flow direction, indicating formation of the string-like assemblies of demixed polymer-rich domains aligned parallel to the flow direction [40,42] as shown by the optical image in Fig. 9b-1 and by a schematic model in Fig. 9b-2. The string-like assemblies were found to exhibit a dramatic increase in their optical anisotropy (negative value of birefringence Δn_{x-z}) with increasing shear rate in the later stage in Regime IV defined as "stage 2" (Fig. 9a): The strings having only weak optical anisotropy in "stage 1" of Regime IV (as schematically shown by the model in Fig. 9b-2) were transformed into those having a strong optical anisotropy in "stage 2" of Regime IV (as schematically shown by the model in Fig. 9b-3) over a narrow shear rate range with increasing shear rate. This transformation implies that a bundle of highly stretched PS chains, which interconnect the domains in the strings, may be formed (Fig. 9b-3). The transformation occurs in parallel to the shear thickening as shown by the upturn in η with $\dot{\gamma}$ (in stage 2 in Fig. 9a). Although the strings are

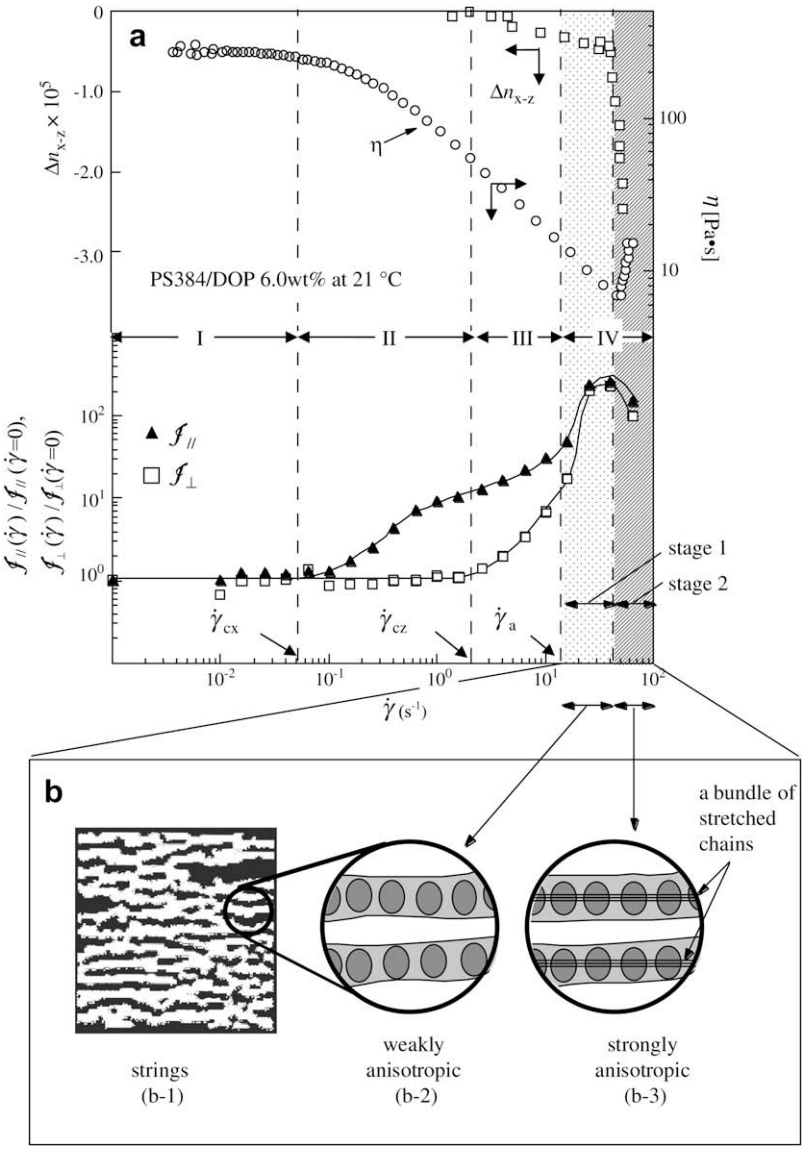

Fig. 9. Birefringence Δn_{x-z}, reduced integrated intensity $\mathcal{I}_{//}(\dot{\gamma};T)/\mathcal{I}_{//}(\dot{\gamma}=0;T)$ and $\mathcal{I}_{\perp}(\dot{\gamma};T)/\mathcal{I}_{\perp}(\dot{\gamma}=0;T)$, parallel and perpendicular to shear flow, respectively, and shear viscosity η (part a) and schematic illustration of the shear-induced string-like structure in Regime IV (part b) for 6.0 wt% PS384/DOP solution at 21 °C (M_w of PS is 3.84×10^6 and the solution has the cloud point of 10 °C). Regime IV indicates a sharp transition from the weakly anisotropic phase of stage 1 (part b-2) to the strongly anisotropic phase of stage 2 (part b-3), probably due to formation of a bundle of stretched chains interconnecting the demixed domains.

the dissipative structures stable under the shear flow, regardless of their strength of optical anisotropy and of whether they are crystalline (as in the case of the PE solution) or not (as in the case of the PS solution), they disappear after cessation of shear, if there are no solidification mechanisms such as crystallization or vitrification and the systems returned into a homogeneous solution for the noncrystallizable PS solutions and for the PE solutions at $T > T_d^0$ (equilibrium melting temperature of crystals in the solution).

In the case of the PE solutions, we found that the above classifications should be changed as follows, depending on temperature. (i) At $T < 147$ °C, Regimes III and IV in the PS solutions degenerated into Regime III_a in the case of the PE solutions where optically anisotropic string-like or fibrous structures (corresponding to the strings having strong optical anisotropy as shown in Fig. 9b-3) are directly formed immediately after the transformation of the shear-enhanced concentration fluctuations to the demixed domains as a steady-state structure, as demonstrated by the sharp increase of birefringence Δn_{x-z} in Fig. 4a, above the critical shear rate $\dot{\gamma}_{c,streak}$; In this case Regime III_a corresponds to Regime IV in the PS solution (Fig. 9a). (ii) At $T \geq 147$ °C (close to equilibrium melting temperature for bulk PE), the PE solutions exhibit only Regime III_b even in the highest shear range accessible in this work where the scattering behaviors are essentially equivalent to those in Regime III in the PS solutions (Fig. 9a): In this case the PE solution never reaches Regime III_a and forms only the demixed domains.

The above fact (i) may be interpreted on the basis of the following transient time-evolution process leading to the steady-state structure: In the case of the PE solutions when demixed structures due to the shear-induced phase separation are formed after step-up shear into Regime III_a, they are expected to align rapidly into string-like domain structures having the weak optical anisotropy and then to be transformed into the optically anisotropic fibrous structures (corresponding to the strings having the strong optical anisotropy). In this series of transient events, the demixed domains, which exist in Regime III in the PS solutions, are considered to exist only as a transient state in the case of the PE solutions

and not to develop into a steady-state structure. In fact this was evidenced by our transient shear rheo-optical experiments [16]. Thus this fact (i) may be considered to be a unique point for the shear-induced structures in the crystallizable solutions. The strings in the PE solution having the strong optical anisotropy did not decay but rather grew after the cessation of shear at 124 °C (see Fig. 8a) presumably because T_d^0 of PE crystals in the solution is higher than 124 °C, and hence the strings developed under the sheared solution were solidified by crystallization. However they decayed very slowly after the cessation of shear at 137 °C (Fig. 8b), which is believed to be due to melting of crystals formed by the shear-induced crystallization.

The fact (ii) described above may be interpreted as a universal feature for shear-induced demixed domain structures for non-crystallizable polymers, because even for the PE solutions under shear, they are noncrystallizable at $T > 146$ °C. At such high temperatures the PE solutions should be so stable that the solution would never be brought to Regime IV in the PS solution or III_a in the PE solution even at the highest accessible shear rates.

We would like to add a brief comment on the effects of the wide molecular weight distribution on the structure formation and the phase diagram. The structure formation occurs due to the elastic effects mediated by the dynamic asymmetry of the constituents comprising the solutions [43,44]. In the semidilute solutions discussed here, the effects of the dynamic asymmetry between polymers and solvent are expected to be larger and hence more significant than the effects of the dynamic asymmetry between different molecular weight polymers. We therefore anticipate that the main characteristics of the phase diagram and the structure formation will not be significantly affected by the polydispersity effects. In the case of polymer melts, however the polydispersity effects will give important effects on the structure formation.

6. Conclusions

The shear small-angle light scattering (shear-SALS) was investigated in order to explore the shear-induced structures developed in the semidilute solution of an ultrahigh molecular weight polyethylene (UHMWPE) over a wide range of T ($>T_{nm}$, the nominal melting temperature of crystals in the quiescent solution) and $\dot{\gamma}$. The scattering behavior elucidated a phase diagram for the shear-induced structure in the T–$\dot{\gamma}$ parameter space as shown in Fig. 6 where Regimes I–III are identified (III being composed of III_a and III_b). The each regime is summarized as follows:

Regime I ($\dot{\gamma} < \dot{\gamma}_{cx}$): The solution under the shear flow is kept to be a homogeneous single-phase solution as a quiescent solution.

Regime II ($\dot{\gamma}_{cx} \le \dot{\gamma} < \dot{\gamma}_{c,streak}$ or $\dot{\gamma}_{cz}$): The butterfly pattern and the shear-induced concentration fluctuations are developed under the flow. The critical shear rate $\dot{\gamma}_{cx}$ is found to be essentially independent of temperature. In this regime, the scattered intensity along the flow direction is enhanced but the intensity along the neutral direction remains the same as the quiescent solution, so that the enhanced concentration fluctuations are essentially characterized by the plane-wave type concentration fluctuations with their wave vectors preferentially oriented along the flow direction.

Regime III: This regime was found to be split into Regime III_a and Regime III_b, depending on temperatures T: Regime III_a at $T \le 146$ °C and Regime III_b at $T > 146$ °C. In Regime III_a, the streak pattern was developed perpendicular to flow in addition to the butterfly pattern. The pattern reflects formation of the optically anisotropic string-like or fibrous crystalline structures having the optical anisotropy. In Regime III_b, however, the streak pattern indicative of the fibrous crystalline structures was not observed even at the highest shear rate covered ($\simeq 10^3\ s^{-1}$). However, the scattered intensity perpendicular to the flow became stronger with $\dot{\gamma}$ and the dark streak of the butterfly pattern became ambiguous with increasing $\dot{\gamma}$. This particular behavior is quite similar to that found in Regime III found for the noncrystallizable PS solutions and hence indicative of shear-induced demixed structures with no significant optical anisotropy or molecular orientation. The solution at $T > 146$ °C is more stable than that at $T \le 146$ °C so that the PE solution even under the higher shear rates behave similarly to the noncrystallizable sheared solution.

It should be noted in Fig. 6 that the boundary between III_a and III_b at $\dot{\gamma} > 30\ s^{-1}$ is very steep in the T–$\dot{\gamma}$ parameter space and approximated by a vertical line around 147 °C. This temperature is apparently close to the equilibrium melting temperature 146 ± 0.5 °C for the bulk high molecular weight linear PE [45]. However we do not know how we can interpret this coincidence at this moment. Our data show that all the streak patterns developed at $133\ °C \le T(°C) \le 146\ °C$ disappear after cessation of the shear. This evidence leads us to interpret T_d^0 for crystals to be developed in the solution is lower than 133 °C. The solid straight line for $\dot{\gamma}_{c,streak}$ appears to be smoothly interconnected with the dotted line interconnecting the cross (X) symbols for $\dot{\gamma}_{cz}$ at $T \ge 146$ °C. We think it is interesting, as a future work, to investigate the wedge-like region marked by W and its surrounding region in the phase diagram shown in Fig. 6. The region W exists in between the dotted line and the dash–dot line where the shear-SALS data are lacking.

In Fig. 6 we tentatively assigned the region W as a part of Regime III_b. This is because the shear-induced crystallizability should decrease with increasing T. As a consequence, a direct transformation from the plane-wave type concentration fluctuations to the crystalline fibrous structures may become less probable with increasing $\dot{\gamma}$ at $T > 135$ °C, on the contrary to the case at $T < 135$ °C where the direct transformation is possible due to a high shear-induced crystallizability. At $T > 135$ °C, the transformation may occur only through Regime III_b where formation of the demixed domains and then their alignment into string-like structures parallel to the flow direction occur.

Although the phase diagram shown in Fig. 6 was determined by changing shear rates at given temperatures. The diagram can be used also to predict effects of shear flows on formation of dissipative structures in the case when temperature is lowered from a high temperature, e.g., 150 °C, at given shear rates in the range of $10^{-3}\ s^{-1} < \dot{\gamma} < 10^3\ s^{-1}$. For example, we can expect the following paths for the change in the dissipative structures: (a) at $\dot{\gamma} > 20\ s^{-1}$, the structure will change from that in III_b to that in III_a; (b) at $6\ s^{-1} < \dot{\gamma} < 20\ s^{-1}$, from II to III_b and eventually to III_a (assuming that the wedge regime W belongs to Regime III_b); (c) at 0.7–$1\ s^{-1} < \dot{\gamma} < 6\ s^{-1}$, from II to III_a, here the lower bound of $\dot{\gamma}$ being estimated as an intercept between the straight line for $\dot{\gamma}_{c,streak}$ and the nominal melting temperature T_{nm} of 120 °C; (d) at $0.06\ s^{-1} < \dot{\gamma} < 0.7$–$1\ s^{-1}$, from II to crystallization below T_{nm}; (e) at $\dot{\gamma} < 0.06\ s^{-1}$, from I to crystallization below T_{nm}. The fibrous crystalline structures formed during the cooling process in the case of (a) to (c) will be different and the differences will elucidate an important effect on the kinetic pathway on the final morphology obtained at low temperatures below T_{nm}. Comparisons of the cases (d) and (e) also will give an intriguing effect on how the shear-enhanced concentration fluctuations influence the final morphology below T_{nm}.

Acknowledgement

The authors express our gratitude to Dr. Takuji Kume for his kind help on our experiments.

References

[1] Murase H, Kume T, Hashimoto T, Ohta Y. Macromolecules 2005;38(15):6656–65.
[2] Hashimoto T. Bull Chem Soc Jpn 2005;78(1):1–39.
[3] Ver Strate G, Phillipoff W. J Polym Sci Polym Lett 1974;12:267–75.
[4] Schumidt R, Wolf BA. Colloids Polym Sci Polym Lett Ed 1979;257(11):1188–95.
[5] Rangel-Nafaile C, Metzner AB, Wissbrun KF. Macromolecules 1984;17(6):1187–95.
[6] Helfand E, Fredrickson GH. Phys Rev Lett 1989;62(21):2468–71.
[7] Milner ST. Phys Rev E 1993;48(5):3674–91.
[8] Onuki A. J Phys Condens Matter 1997;9(29):6119–57.
[9] Hashimoto T, Fujioka K. J Phys Soc Jpn 1991;60(2):356–9.
[10] Wu XL, Pine DJ, Dixon PK. Phys Rev Lett 1991;66(18):2408–11.
[11] Yanase H, Moldenaers P, Mewis J, Abetz V, van Egmond J, Fuller GG. Rheol Acta 1991;30(1):89–97.
[12] Hashimoto T, Kume T. J Phys Soc Jpn 1992;61(6):1839–43.
[13] Van Egmond JW, Fuller GG. Macromolecules 1993;26(26):7182–8.
[14] Kume T, Hattori T, Hashimoto T. Macromolecules 1997;30(3):427–34.
[15] Murase H, Kume T, Hashimoto T, Ohta Y, Mizukami T. Macromolecules 1995;28(23):7724–9.
[16] Murase H, Kume T, Hashimoto T, Ohta Y. Macromolecules 2005;38(21):8719–28.
[17] McHugh AJ. In: Lyngaae-Jørgensen J, Søndergaard K, editors. Rheo-physics of multiphase polymeric systems. Lancaster, PA: Technomic Publishing; 1995 [chapter 6].
[18] Mitsuhashi S. Bull Text Res Inst (J) 1963;66:1.
[19] Pennings AJ, Kiel AM. Kolloid ZZ Polym 1965;205(2):160–2.
[20] Pennings AJ, van der Mark JMAA, Booij HC. Kolloid ZZ Polym 1969;236(2):99–111.
[21] Keller A, Willmouth FM. J Macromol Sci 1972;B6(3):539–44.
[22] Pennings AJ. J Polym Sci Polym Symp 1977;59:55–86.
[23] McHugh AJ, Spevacek JA. J Polym Sci Part B Polym Phys 1991;29(8):969–79.
[24] Keller A, Kolnaar HWH. In: Meijer HEH, editor. Processing of polymers, vol. 18. New York: VCN; 1997. p. 189.
[25] de Gennes PG. J Phys Chem 1974;60(12):5030–42.
[26] Seki M, Thurman DW, Oberhauser JP, Kornfield JA. Macromolecules 2002;35(7):2583–94.
[27] Yang L, Somani RH, Sics I, Hsiao BS, Kolb R, Fruitwala H, et al. Macromolecules 2004;37(13):4845–59.
[28] Somani RH, Yang L, Zhu L, Hsiao BS. Polymer 2005;46(20):8587–623.
[29] Ogino Y, Fukushima H, Matsuba G, Takahashi N, Nishida K, Kanaya T. Polymer 2006;47:5669–77.
[30] Kimata S, Sakurai T, Nozue Y, Kasahara T, Yamaguchi N, Karino T, et al. Science 2007;316:1014–7.
[31] Balzano L, Kukalyekar N, Rastogi S, Peters GWM, Chadwick JC. Phys Rev Lett 2008;100:048302.
[32] Dukovski I, Muthukumar M. J Chem Phys 2003;118(14):6648–55.
[33] (a) Hashimoto T, Murase H, Ohta Y. Macromol Symp 2009;279:88–95; (b) Hashimoto T. In the extended abstract, Macro2008, Taipei; 2008.
[34] Hoffman JD, Weeks JJ. J Res Natl Bureau Standard – A, Phys Chem 1962;66A(1):13–28.
[35] Hashimoto T, Takebe T, Suehiro S. Polym J 1986;18(2):123–30.
[36] Kume T, Asakawa K, Moses E, Matsuzaka K, Hashimoto T. Acta Polym 1995;46:79–85.
[37] Saito S, Hashimoto T, Morfin I, Lindner P, Boue F. Macromolecules 2002;35(2):445–59.
[38] We should note that there is a mismatch between the scattering behavior shown in Fig. 2 and that shown in Fig. 4. In Fig. 2 the pattern #3 taken at 124 °C and at shear rate $\dot{\gamma} = 1.15\ s^{-1}$ and the pattern #6 taken at 133 °C and at $\dot{\gamma} = 2.9\ s^{-1}$ show the streak pattern, whereas the integrated intensity $\mathcal{I}_{\perp}$ corresponding to those points (T, $\dot{\gamma}$) still keeps the same or almost the same value as that in quiescent solution in Fig. 4. This difference arises from the differences in experimental conditions employed to obtain the results shown in Figs. 2 and 4. In the experiments in Fig. 2, the shear was imposed on the system at one step from zero shear rate to a given shear rate. In the case of Fig. 4, on the contrary, a multi-step shear, instead of the one step, was imposed on the solution as follows; the scattered intensity at each given shear rate was measured after the intensity reached a constant value, and then the shear rate was increased to a next higher shear rate. This difference in experimental condition may give rise to a difference in total strain in the two experimental condition and thereby a slight variation in the critical shear rate $\dot{\gamma}_{c,streak}$ which was defined as the boundary between Regimes II and III as shown in Fig. 4.
[39] Saito S, Hashimoto T. J Chem Phys 2001;114:10531.
[40] Kume T, Hashimoto T, Takahashi T, Fuller GG. Macromolecules 1997;30(23):7232–6.
[41] Endoh MK, Takenaka M, Inoue T, Watanabe H, Hashimoto T. J Chem Phys 2008;128:164911.
[42] Kume T, Hashimoto T. ACS Symp Series, Am Chem Soc 1995;597:35–47.
[43] Doi M, Onuki A. J Phys II 1992;2:1631.
[44] Onuki A. J Non-Cryst Solids 1994;172:1151.
[45] Mandelkern L. J Phys Chem 1967;71:3833.